Check for updates

Received: 15 July 2025 | Revised: 24 December 2025 | Accepted: 11 January 2026

DOI: 10.1002/aic.70238

AIChE JOURNAL

RESEARCH ARTICLE

Biomolecular Engineering, Bioengineering, Biochemicals, Biofuels, and Food

A rational strategy to optimize photodrugs by Molecular Dynamics simulations for killing drug-resistant Gram-negative bacteria

Lei Hao[1,2] | Yeonho Song[3] | Cheng Zhang[2] | Yumei Wang[2] | Haoying Ge[4] | Wen Sun[1] | Jingyun Wang[1,2] | Jun Soo Kim[3] | Xiaojun Peng[1] | Juyoung Yoon[3,5] | Haidong Li[1,2]

[1]State Key Laboratory of Fine Chemicals, Frontiers Science Center for Smart Materials Oriented Chemical Engineering, Dalian University of Technology, Dalian, Liaoning, China

[2]MOE Key Laboratory of Bio-Intelligent Manufacturing, School of Bioengineering, Dalian University of Technology, Dalian, Liaoning, China

[3]Department of Chemistry and Nanoscience, Ewha Womans University, Seoul, Korea

[4]School of Chemistry and Chemical Engineering, Linyi University, Linyi, China

[5]Graduate Program in Innovative Biomaterials Convergence, Ewha Womans University, Seoul, Korea

Correspondence
Jun Soo Kim and Juyoung Yoon, Department of Chemistry and Nanoscience, Ewha Womans University, Seoul 03760, Korea.
Email: jkim@ewha.ac.kr and jyoon@ewha.ac.kr

Haidong Li, State Key Laboratory of Fine Chemicals, Frontiers Science Center for Smart Materials Oriented Chemical Engineering, Dalian University of Technology, 2 Linggong Road, Dalian 116024, Liaoning, China.
Email: lihd@dlut.edu.cn

Funding information
National Key Research and Development Program of China, Grant/Award Number: 2023YFB3810300; National Natural Science Foundation of China, Grant/Award Numbers: 22378050, 22378051, 22090011; Liaoning Provincial Science and Technology Joint Fund, Grant/Award Number: 2023JH2/101700296; Fundamental Research Funds for the Central Universities, Grant/Award Numbers: DUT24ZD117, DUT24LAB105; National Research Foundation of Korea, Grant/Award Numbers: RS-2023-00217701, 2022R1A2C3005420, 2020R1A5A2019210

[Correction added on 5 March 2026, after first online publication: The copyright line was changed.]

Abstract

Antimicrobial resistance has become a major threat to human health, particularly for Gram-negative bacteria such as *Acinetobacter baumannii* and *Klebsiella pneumoniae*. Disruption of membrane integrity is regarded as a promising antimicrobial strategy that does not induce distinct drug resistance, while increasing the internalization of drug doses and mitigating efflux mechanisms. In this study, relying on molecular dynamics (MD) simulations to optimize and confirm the membrane-disrupting activity of photodrugs, we fabricated a series of monomeric (TC_n) and dimeric (TC_nT) photodrugs ($n = 4$, 8, 12, and 16), with different alkyl chain lengths, enabling their differing bacterial membrane rupture capabilities of inherent. Notably, based on MD simulations and *in vitro* experiments, TC_8T exhibited enhanced antibacterial efficacy against multiple drug-resistant Gram-negative strains upon white light irradiation, including clinically difficult-to-treat strains. More importantly, TC_8T demonstrated robust antimicrobial activity and promoted tissue reconstruction in murine models of wound infection and post-tumor-resection mixed infections.

KEYWORDS
drug-resistant pathogens, membrane disruption, molecular dynamics simulations, photodrugs, photon-driven therapy

Lei Hao and Yeonho Song contributed equally to this work.

This is an open access article under the terms of the Creative Commons Attribution-NonCommercial License, which permits use, distribution and reproduction in any medium, provided the original work is properly cited and is not used for commercial purposes.
© 2026 The Author(s). *AIChE Journal* published by Wiley Periodicals LLC on behalf of American Institute of Chemical Engineers.

1 | INTRODUCTION

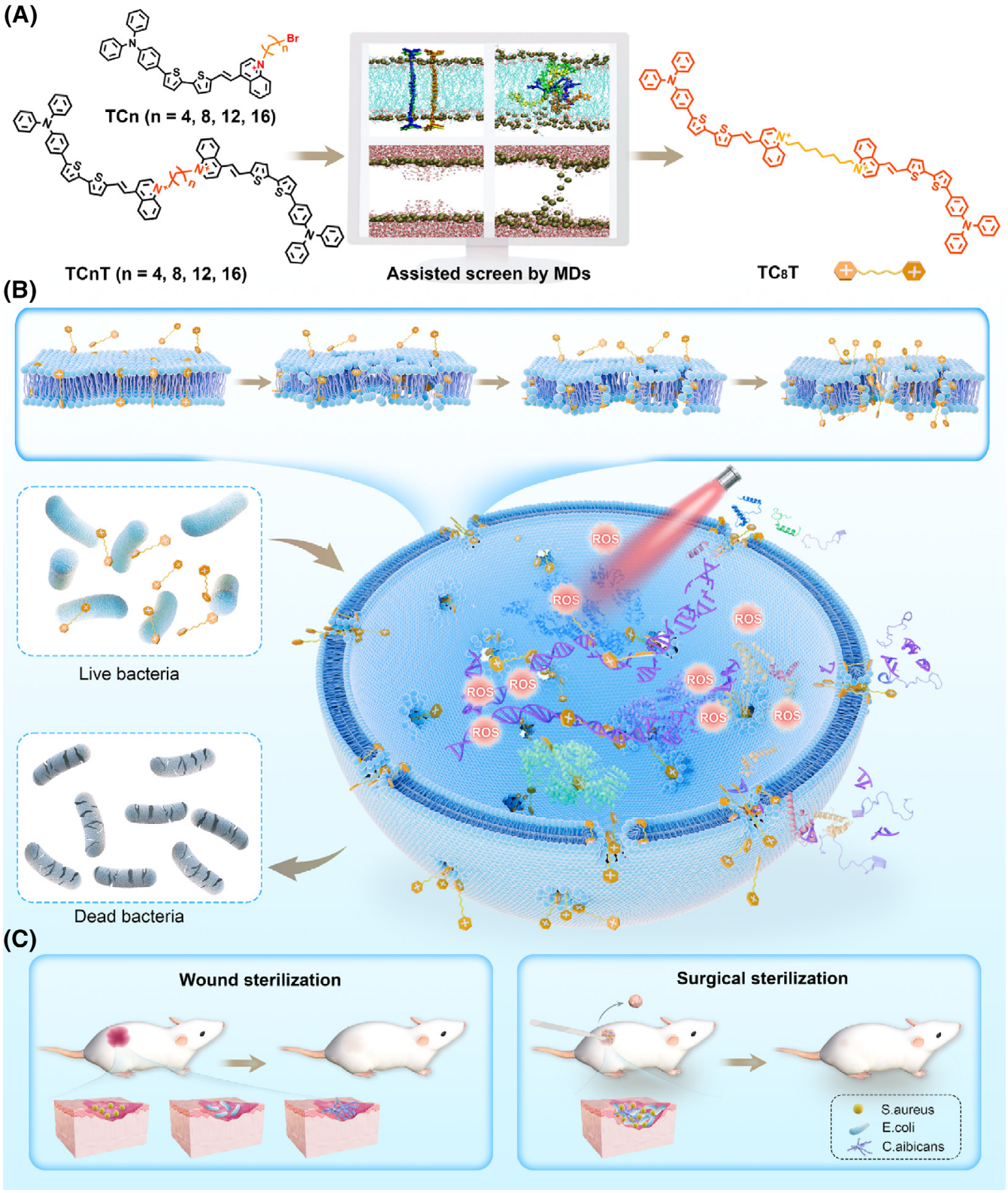
Antibiotic-resistant bacterial infections are a major global health problem, causing millions of deaths worldwide each year.[1,2] According to The Lancet (2024), bacterial drug-resistant infections, or antimicrobial resistance, are now the third leading cause of death globally, behind heart disease and stroke, and surpassing deaths caused by Human Immunodeficiency Virus/Acquired Immunodeficiency Syndrome (HIV/AIDS), breast cancer, and malaria.[2,3] While the discovery of antibiotics in the last century undeniably saved countless lives, the increasing pressure on clinical medications caused by the overuse of antibiotics has accelerated the growth and spread of bacterial resistance.[4] This dilemma has inevitably led to the antimicrobial resistance crisis, which has significantly impacted clinical drug choices and imposed severe economic costs. As reported in the 2024 World Health Organization Bacterial Priority Pathogens List (BPPL), Gram-negative bacteria, such as *Acinetobacter baumannii* (*A. baumannii*) and various Enterobacteriaceae (e.g., extended-spectrum beta-lactamase [ESBL] *Escherichia coli*),[5] are listed as critical priorities, posing a significant healthcare burden globally due to their ability to transfer drug-resistant genes and the severity of the infections and diseases they cause.[6–10] Despite tremendous efforts in recent decades, the development of novel antibiotics with superior potency, safety, and acceptable pharmacokinetic profiles remains stagnant globally, primarily due to the highly dense organizational structure of Gram-negative bacterial membranes, which effectively inhibits the binding and penetration of foreign invaders. Disruption of membrane integrity, resulting in an increased drug load and mitigation of the efflux mechanism, is regarded as an ideal antimicrobial strategy.[11–18] Thus, designing new antibacterial agents with intrinsic membrane disruption properties is a promising approach for combatting drug-resistant bacteria,[19,20] especially Gram-negative-resistant strains. However, the molecular structure design that endows these agents with inherent membrane destruction capabilities remains unclear, and very difficult.

Recent advances in molecular dynamics (MD) simulations have significantly enhanced our understanding of bacterial membrane systems, providing a valuable tool for studying drug-membrane interactions and guiding the development of antimicrobial agents, while substantially reducing time and costs.[21–24] For instance, Wadhwa et al.,[24] utilized MD simulations to explore the membrane permeability of two structurally similar natural drugs, withaferin-A and withanone, which exhibited significantly different cytotoxicity. The simulations predicted higher permeation for withaferin-A, which was validated experimentally through antibody-based detection and time-lapse fluorescence analysis. Additionally, computational approaches using MD simulations have played a critical role in elucidating the molecular mechanisms by which small molecules interact with bacterial cell membranes, thereby facilitating the development of novel antimicrobial drugs.

In recent years, various types of antimicrobial agents, including synthetic polymers,[25] antimicrobial peptides,[26] metal/metal oxide formulations,[27] carbon-based materials, and photosensitizing drugs, have been explored in response to the crisis of drug resistance in Gram-negative bacteria.[28] Among these, photodynamic therapy (PDT) is a medically approved approach for treating various diseases by exposing patients to light,[19,22,29–31] typically combining harmless, low-intensity light with photosensitizers (also called photodrugs) to enhance the therapeutic effects of light.[1,29,31,32] For PDT, photodrugs play a critical role as they exert cytotoxic effects on pathogenic microorganisms by generating highly toxic reactive oxygen species (ROS), including singlet oxygen ($^1O_2$) and superoxide ($O_2^{\bullet-}$). Consequently, PDT holds great potential as a new alternative therapy against clinical antibiotic resistance. The main advantages of antimicrobial phototherapy include (1) its noninvasive and cost-effective nature, (2) the convenience of daily operation, and (3) its suitability for repeated application without causing resistance.[22,33–36] With the development of effective phototherapeutic agents and advanced optical technologies, photon-driven therapy shows promise for the treatment of microbial infections, especially those caused by multidrug-resistant bacteria. However, the limited ability of photodrugs to penetrate the bacterial barrier,[15,30,37–39] particularly in inherently disrupting membrane integrity, further restricts the clinical application of antimicrobial outcomes. Therefore, the rational structural design of photodrugs capable of perturbing the bacterial membrane is particularly important in the pursuit of optimal antimicrobial phototherapy, yet remains a vital challenge.

Herein, to develop effective antibacterial photodrugs, we designed a series of monomeric and dimeric cationic photodrugs by modulating the size of the alkyl chain structure to obtain TC_n and TC_nT ($n = 4$, 8, 12, and 16), as shown in Scheme 1. We conducted multiple sets of MD simulations to evaluate and optimize their ability to embed into membranes and disrupt their structures. The simulation results revealed that membrane disruption is strongly influenced by the synthetic effects of cationic charges and molecular size, with TC_8T exhibiting the highest membrane-disruptive potential. In this study, the potential of mean force (PMF) calculated using the umbrella sampling method represents the free energy change ΔG required for the photodrugs to move from solution to a specific position within the bilayer. The PMF calculations show that TC_8T can spontaneously insert into the membrane bilayer due to its large free energy change ΔG. In addition, the matching size of the TC_8T molecule facilitates the membrane disruption more effectively, then more TC_8T enrichment onto the bacterial membrane and into the interior. To validate the results obtained from MD simulations, comprehensive evaluation using confocal laser scanning microscopy (CLSM), scanning electron microscopy and *in vitro* inhibitory plate coating further were confirmed. More exciting, the MD simulation results were cross-verified with the experimental results, the TC_8T is most effective in dealing with Gram-negative bacterial infections. Upon photoirradiation, TC_8T exerts photosensitizing activity through both type I and type II mechanisms, generating highly toxic ROS, including $^1O_2$ and $O_2^{\bullet-}$, which further aggravate bacterial structural damage. Combining its intrinsic membrane disruption ability and efficient phototoxicity, TC_8T provides excellent antimicrobial efficacy against multidrug-resistant Gram-negative bacteria (*A. baumannii*, *Klebsiella pneumoniae*, and ESBL *Escherichia coli*). To validate the clinical potential of TC_8T, we tested it in the mouse wound infection models, where TC_8T showed outstanding antibacterial activity in this case. Moreover, TC_8T also inhibited wound bacterial colonization and promoted wound healing in a mouse model of mixed bacterial infection following tumor

15475905, 2026, 5, Downloaded from https://aiche.onlinelibrary.wiley.com/doi/10.1002/aic.70238 by Ewha Womans University Library, Wiley Online Library on [21/09/2026]. See the Terms and Conditions (https://onlinelibrary.wiley.com/terms-and-conditions) on Wiley Online Library for rules of use; OA articles are governed by the applicable Creative Commons License



SCHEME 1 (A) Schematic diagram of molecular dynamics simulation-assisted screening of the monomeric and dimeric photodrugs TC_n and TC_nT ($n = 4$, 8, 12, and 16). (B) Schematic diagram of the antimicrobial mechanism of the dimeric photodrugs. (C) Applications of TC_8T for the treatment of multiple model bacterial infections.

resection, clearly demonstrating its potential for future clinical application. These results highlight the success of our strategy in developing a new generation of dimeric antimicrobial photodrugs, where the novelty lies in integrating MD simulations with experimental validation to guide the design and evaluation of newly developed cationic photodrugs. In particular, the effect of dimeric photodrugs on bacterial membrane

15475905, 2026, 5, Downloaded from https://aiche.onlinelibrary.wiley.com/doi/10.1002/aic.70238 by Ewha Womans University Library, Wiley Online Library on [21/09/2026]. See the Terms and Conditions (https://onlinelibrary.wiley.com/terms-and-conditions) on Wiley Online Library for rules of use; OA articles are governed by the applicable Creative Commons License

structures offers a promising approach to addressing the pressing clinical problem of antibiotic resistance.

2 | MATERIALS AND METHODS

2.1 | MD simulations

We performed MD simulations using GROMACS 2020[40,41] and visualized the results with Visual Molecular Dynamics (VMD).[42] The inner membrane of Gram-negative bacteria was modeled as a 3:1 mixture of 1-palmitoyl-2-oleoyl-sn-glycero-3-phosphatidylethanolamine (POPE) and 1-palmitoyl-2-oleoyl-sn-glycero-3-phosphatidylglycerol (POPG),[43,44] constructed via CHARMM-GUI.[45,46] The CHARMM36 force field[47] was used for lipids and ions, and the CGenFF server[48] provided the parameters for the photodrugs (TC_n and TC_nT). The system was solvated with the TIP3P water model and neutralized with 0.150 M KCl.

MD simulations were carried out to (i) examine the spontaneous insertion of TC_n and TC_nT into the lipid bilayer, (ii) compute the PMF along the membrane normal, and (iii) characterize their effect on the lipid bilayer when embedded within the membrane. Details of the simulation systems, parameters, and PMF calculation method are provided in Supporting Information S1.

2.2 | Materials and instrumentation

All general chemicals for fluorescence detection and organic synthesis including dihydrorhodamine 123 (DHR123), ABDA (9,10-anthracenediyl-bis[methylene]dicarboxylic acid), and 2,7-dichlorodihydrofluorescein (DCFH) were purchased from Energy Chemical Co. (Shanghai, China). ^{1}H Nuclear Magnetic Resonance (NMR) and ^{13}C NMR spectra were obtained using Bruker NMR spectrometers. High-resolution mass spectra (HRMS) were recorded on an Agilent G6224A (USA). Determination of the Ultraviolet-visible (UV)–visible absorption broad spectrum was performed using an Agilent UV (USA) spectrophotometer. The determination of the fluorescence emission broad spectrum was recorded using a spectrofluorophotometer. A Zeiss LSM 980 (Germany) laser scanning confocal microscope was used for CLSM image collection. SpectraMax M2e (USA) fully automated plate reader was used for the determination of solution absorbance. A xenon lamp unit was used for light illumination in this experiment. Nanoparticle particle size and zeta potential analysis was performed using a Malvern Zeta sizer Nano-S90 (UK). Self-assembled nanoparticles of compounds in aqueous solution were imaged using a field emission transmission electron microscope JEM-F200 (Japan). Bacterial morphology was analyzed using a HITACHI SU5000 (China) field emission scanning electron microscope. Yeast extract, tryptone and agar were purchased from OXOID (Shanghai, China).

2.3 | Scanning electron microscope observation of bacteria

E. coli was incubated with 2 μM photodrugs for 1 h and irradiated with white light (10 mW/cm^2) for 10 min. The irradiated bacterial fluids were fixed with 2.5% glutaraldehyde at 4°C overnight and dehydrated with an ethanol gradient. Two microliters of the bacterial solution was immobilized on a silicon wafer, subsequently sprayed with gold, and observed in a HITACHI SU5000.

2.4 | Mouse infection model

Female Balb/c mice (6–7 weeks old) were provided by Shenyang Changsheng Biologicals for the experiments. The dorsal wound infection model was established by cutting wounds through the back and inoculating cultured *E. coli* (1×10^8 Acolony-forming unit (CFU), 1.50 μL) into the dorsal wounds of the mice. 4T1 (1×10^6) cells were inoculated into the backs of mice, the tumors were cultured for 7 days, then the tumors were surgically excised, and a triple coating of cultured *E. coli*, *Staphylococcus aureus*, and *Candida albicans* (1×10^8 CFU) was applied 1.5 μL to inoculate into the surgical incision to establish a model of postoperative cross-infection. All the animal experiments involved in this study were conducted in accordance with the Guide for the Care and Use of Laboratory Animals published by the US National Institutes of Health (8th edition, 2011), and approved by the local research ethics review board of the Animal Ethics Committee of Dalian University of Technology.

Synthesis procedures and characterization data, ROS-generating ability test, cultivation and preparation of strains, *in vitro* cytotoxicity assay, *in vitro* antimicrobial assays, *in vivo* antimicrobial assays, and statistical analysis were put in Supporting Information S1 section.

3 | RESULTS AND DISCUSSION

3.1 | MD simulation

Advancements in computational chemistry and biophysics have significantly enhanced the reliability of computational models of cell membranes, making the computational assessment of potential antibacterial photodrugs, as well as the verification of their antibacterial mechanisms, both rapid and effective. Therefore, design, prediction, and analysis through MD simulations help reduce unnecessary testing of antibacterial photodrugs, contribute to a comprehensive understanding of their intrinsic antibacterial mechanisms, and establish new approaches for constructing next-generation photodrugs. In this study, we integrated MD simulations into both the design and evaluation process of a new series of cationic photodrugs, enabling a rational and predictive approach to their development.

We designed a series of monomeric photodrugs TC_n ($n = 4$, 6, 12, and 16, Figures 1A and S1), with antibacterial potential. Building on TC_n, we also proposed a design scheme for the dimeric photodrugs TC_nT (Figures 1A and S1) to further explore the antimicrobial mechanisms of photodrugs with varying cationic charges and molecular sizes. The antibacterial feasibility and intrinsic mechanisms of action of TC_n and TC_nT were initially evaluated using MD simulations. Specifically, three sets of MD simulations for TC_n and TC_nT were

15475905, 2026, 5, Downloaded from https://aiche.onlinelibrary.wiley.com/doi/10.1002/aic.70238 by Ewha Womans University Library, Wiley Online Library on [21/09/2026]. See the Terms and Conditions (https://onlinelibrary.wiley.com/terms-and-conditions) on Wiley Online Library for rules of use; OA articles are governed by the applicable Creative Commons License

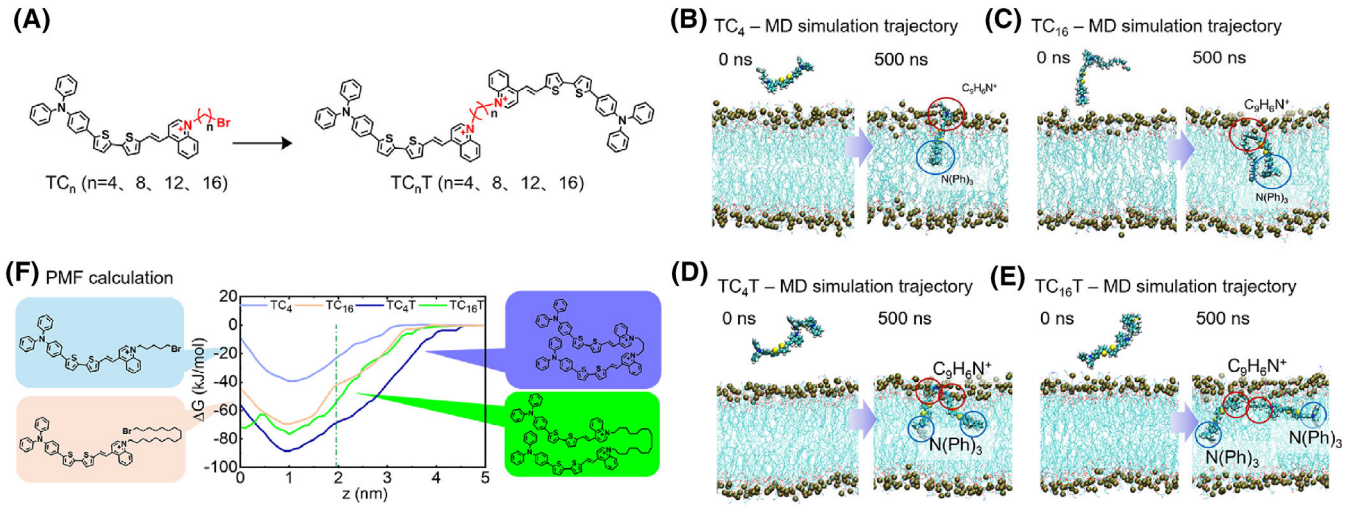


FIGURE 1 (A) Monomeric molecular structures of TC_n and the synthesis process of dimeric photodrugs TC_nT ($n = 4$, 8, 12, and 16). (B–E) 500-ns molecular dynamics (MD) simulation trajectories of monomeric photodrugs TC_4 and TC_{16}, and dimeric photodrugs TC_4T and $TC_{16}T$, showing the locations of the $N(Ph)_3$ and $C_9H_6N^+$ groups within the membrane. (F) Potential of mean force for the insertion and escape of photodrugs TC_4, TC_{16}, TC_4T, and $TC_{16}T$, illustrating spontaneous photodrugs insertion and the energy barrier for these compounds. The value $z = 0$ on the abscissa represents the center of the lipid bilayer, while $z = 2$ marks the bilayer boundary, as defined by the location of lipid P atoms.

conducted. First, to confirm the spontaneous insertion of the photodrugs into the bacterial membrane, their insertion into the lipid bilayer was investigated. In this work, the bacterial membrane is modeled using a lipid bilayer composed of POPE:POPG = 3:1.[21,43,44] Second, we calculated the PMF of the photodrugs along the direction perpendicular to the membrane, providing a quantitative comparison for their thermodynamic tendency for insertion into and escape from the membrane.[49] Finally, the stability of the membrane in the presence of incorporated photodrugs was investigated. These MD simulations can provide insights into whether the photodrugs can successfully embed into the membrane and disrupt its structure, both of which are critical for effective antimicrobial activity. The MD simulations were conducted using GROMACS v2020.4 and the bilayer structures were prepared using CHARMM-GUI.[40,41,47,50] The force fields of all photodrugs, TC_n and TC_nT, were generated using CGgenFF homepage.[48] Simulation details are provided in Supporting Information S1 section.

We conducted 500-ns MD simulations to investigate the insertion of photodrugs into the lipid bilayer. All photodrugs, initially positioned slightly above the lipid bilayer, spontaneously inserted into the membrane during the simulations. The centers of mass of the photodrugs were located approximately 1 nm above the bilayer center, as illustrated in Figures 1B–E and S2–S5. Upon insertion, the $N(Ph)_3$ groups of the photodrugs were positioned deep within the hydrophobic lipid tails, closer to the bilayer center, due to the hydrophobic nature of the phenyl groups. In contrast, the quinolinium groups were located nearer to the negatively charged lipid head groups, which can be attributed to electrostatic interactions. These results indicate that all TC_n and TC_nT photodrugs can spontaneously insert into the membrane, with their conformations dictated by interactions with lipid molecules.

However, these simulations are limited to verifying the spontaneous insertion of photodrugs into the lipid bilayer, and the complete translocation of the photodrugs across the bilayer could not be observed due to the limited simulation duration. Thermodynamic information about photodrug insertion and subsequent escape from the bilayer is often obtained by calculating the PMF. In this work, the PMF represents the free energy change ΔG required to move the photodrug from the solution to a specific location within the bilayer, and it was calculated using the umbrella sampling method. By comparing the ΔG values at two different locations, the free energy change associated with displacing photodrugs between these locations can be estimated, providing a quantitative understanding of photodrug insertion and escape processes. The ΔG values of the monomeric photodrugs TC_4 and TC_{16} and the dimeric photodrugs TC_4T and $TC_{16}T$ are presented in Figure 1F. Starting from $z = 5$ nm, the ΔG values decrease until reaching their energy minima at approximately $z = 1$ nm, then increase again as z approaches the bilayer center at $z = 0$ nm. The location of the energy minima at $z = 1$ nm, positioned above the bilayer center, is consistent with results from the 500 ns-long MD simulations. The slight increase in ΔG from the energy minimum ($z = 1$ nm) to the bilayer center ($z = 0$ nm) suggests that the center-of-mass position of each photodrug is slightly biased toward one leaflet of the bilayer, rather than being located exactly in the middle of the bilayer. However, the energy barrier from $z = 1$ to $z = 0$ nm was estimated to be 26 kJ/mol and was not prohibitively large, allowing the photodrugs to occasionally transition from one leaflet to the other.

The overall decreases in ΔG from the solution ($z = 5$ nm) to the interior of the bilayer ($z < 5$ nm) indicates that photodrug insertion is thermodynamically favorable and occurs spontaneously. Conversely, the same free energy profile can be interpreted differently when

15475905, 2026, 5, Downloaded from https://aiche.onlinelibrary.wiley.com/doi/10.1002/aic.70238 by Ewha Womans University Library, Wiley Online Library on [21/09/2026]. See the Terms and Conditions (https://onlinelibrary.wiley.com/terms-and-conditions) on Wiley Online Library for rules of use; OA articles are governed by the applicable Creative Commons License

considering the reverse direction: the increase in ΔG from the bilayer interior (z < 5 nm) to the solution ($z = 5$ nm) represents an energy barrier that must be overcome for an inserted photodrug to escape the bilayer.[22] The energy barriers, estimated as the differences in ΔG between $z = 1$ nm (the free energy minimum) and $z = 5$ nm (the solution), are substantial: 39.4, 69.8, 88.4, and 76.6 kJ/mol for TC_4, TC_{16}, TC_4T, and $TC_{16}T$, respectively, corresponding to approximately 15 k_BT, 27 k_BT, 34 k_BT, and 30 k_BT at 310 K. While these significant energy barriers suggest that the photodrugs preferentially remain within the bilayer, occasional stochastic escape from the bilayer is also possible, with TC_4 being the most likely to escape due to its relatively low barrier. Consequently, the monomeric photodrug with the shortest alkyl chain, TC_4, shows the highest likelihood of penetrating across the cell membrane, whereas the monomeric photodrug with a longer alkyl chain, TC_{16}, and the dimeric photodrugs, TC_4T and $TC_{16}T$, are more likely to remain embedded within the bilayer.

While designing these photodrugs, we hypothesized that strong interactions between the photodrugs and lipid molecules would disrupt bacterial cell membranes, thereby facilitating drug loading and mitigating the efflux mechanism. To verify this hypothesis, 1-μs simulations were conducted in order to investigate the effects of inserted photodrugs on membrane structure. For each photodrug, four molecules were positioned within the bilayer, aligned vertically and perpendicular to the bilayer, as shown in Figures 2A,B, S6, and S7. For TC_n, two molecules were oriented upward and the other two downward, while for TC_nT, all four molecules were stretched across the bilayer. These initial configurations ensured electrostatic interactions between the photodrugs' quinolinium groups and the lipid head groups, as well as hydrophobic interactions between the photodrugs' alkyl chains and the lipid tail groups.

Our simulation results revealed that the dimeric photodrugs, TC_nT, effectively disrupt membrane structure, whereas the monomeric photodrugs TC_n, have no significant impact. During 1-μs MD simulations, bilayers embedded with TC_8T, $TC_{12}T$, and $TC_{16}T$ exhibited significant structural disruption, with lipid molecules near the quinolinium cations and accompanying water molecules being drawn into the bilayer. These dimeric photodrugs stretch across the bilayer center, as shown in Figures 2B and S7b–d, and their two quinolinium cations, separated by sufficiently long alkyl chains, strongly interact with the negatively charged lipid head groups of both leaflets. The strong attractive interactions between the quinolinium cations and the lipid head groups were confirmed by the radial distribution function

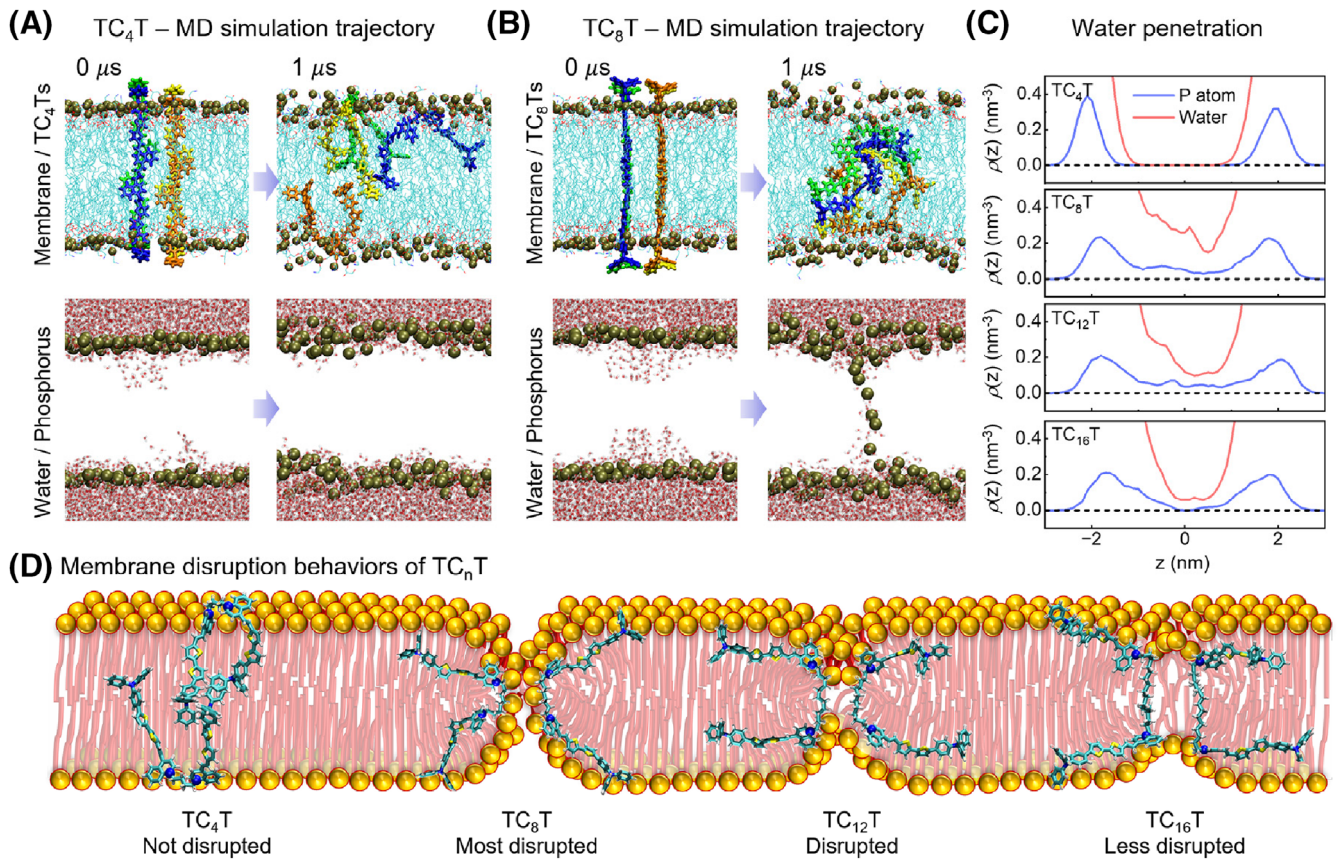


FIGURE 2 (A, B) Snapshots from molecular dynamics (MD) simulations of photodrugs TC_4T and TC_8T, initially aligned within the membrane. The bottom halves of the figures display only lipid P atoms and water molecules, illustrating lipid and water penetration. (C) Average number densities, ρ_P and ρ_W, of lipid P atoms and water molecules, respectively, calculated during the final 500 ns of the 1 μs simulations, highlighting significant membrane disruption caused by photodrugs TC_8T, $TC_{12}T$, and $TC_{16}T$. Complete number density profiles are provided in Figure S9. (D) Illustrations of membrane disruption caused by photodrugs TC_4T, TC_8T, $TC_{12}T$, and $TC_{16}T$.

15475905, 2026, 5, Downloaded from https://aiche.onlinelibrary.wiley.com/doi/10.1002/aic.70238 by Ewha Womans University Library, Wiley Online Library on [21/09/2026]. See the Terms and Conditions (https://onlinelibrary.wiley.com/terms-and-conditions) on Wiley Online Library for rules of use; OA articles are governed by the applicable Creative Commons License

between the N atom in the quinolinium cation and the P atom in the lipid head groups, showing a first peak at $r = 0.4$ nm, as shown in Figure S8a. Due to fluctuations in photodrug conformations, lipid molecules interacting with the quinolinium cations are drawn into the bilayer from both leaflets, along with water molecules. Although TC_4T also contains two quinolinium cations, the separation between them, mediated by its short alkyl chain, is insufficient for both cations to interact with lipid head groups on opposite leaflets. Consequently, TC_4T adopts a bent structure, residing within a single leaflet and failing to draw lipid molecules into the bilayer. These findings underscore the importance of the alkyl chain length, as shown in Figure S8b, consistent with observations by Zheng et al.[22] Conversely, the monomeric photodrugs TC_n ($n = 4$, 8, 12, and 16) behave similarly to TC_4T. With only one quinolinium cation, these monomeric photodrugs reside within a single leaflet without drawing lipid molecules into the bilayer.

The extent of membrane disruption was quantitatively assessed by calculating the number density of lipid P atoms (ρ_P) and water molecules (ρ_W) within the bilayer, as shown in Figures 2C and S9. For photodrugs TC_4T as well as TC_n ($n = 4$, 8, 12, and 16), the membrane structure remained unchanged, with $\rho_P(z = 0) = 0$ and $\rho_W(z = 0) = 0$. In contrast, the values of ρ_P and ρ_W within the bilayer were non-zero for photodrugs TC_8T, $TC_{12}T$, and $TC_{16}T$, with the maximum observed for TC_8T, as indicated by the average numbers of P atoms and water molecules in the central region of the lipid bilayer (see Table 1). In summary, the membrane disruption, as confirmed by the penetration of lipid and water molecules during the 1 μs simulations, followed the order: $TC_8T > TC_{12}T > TC_{16}T$ (Figure 2D). These simulation results underscore the critical role of both hydrocarbon chain length and dual-cation segments in the dimeric photodrug structures for effective membrane disruption.

3.2 | Photodrug synthesis and photophysical properties

Building upon insights from MD simulations, we conducted additional experiments to prepare and characterize the photodrugs TC_n and TC_nT ($n = 4$, 8, 12, 16), aiming to explore their photophysical properties. The synthetic routes for TC_n and TC_nT are depicted in Figure S1. First, their molecular structures were confirmed by NMR spectroscopy and high-resolution mass spectrometry (Figures S10–S37). UV–Vis absorption spectroscopy and fluorescence spectroscopy were then used to characterize their photophysical properties. The photodrugs TC_n and TC_nT employ triphenylamine unit as the donor, a bis-thiophene structure as the molecular π-bridge, and a quinoline cation as the electron acceptor. This configuration facilitates the separation between the highest occupied molecular orbital and lowest unoccupied molecular orbital and promotes electron transfer within the moiety as well as increasing the Stokes shift of the photodrugs. As observed in Figure 3A, TC_n and TC_nT exhibited similar absorption peaks at 535 nm in Dimethyl sulfoxide (DMSO) solution.

TABLE 1 Average numbers of P atoms and water molecules within the z-range of −1.0 to 1.0 nm, chosen to include the central region of water penetration into the lipid bilayer. The values were calculated by integrating the number density profiles, $\rho(z)$, shown in Figure 2C, and multiplying by the xy-planar area of the simulation box.

Photodrug	TC_4T	TC_8T	$TC_{12}T$	$TC_{16}T$
P atom	0.02	5.59	5.30	3.73
Water	0.35	31.53	22.72	22.65

As shown in Figures 3B,C and S38, photodrugs exhibited minimal fluorescence emission in DMSO solution, which was sharply enhanced as the toluene (a poor solvent) fraction of the solution increased to 99%, clearly demonstrating typical aggregation-induced emission characteristics. Absorbance changes in different solutions were analyzed using an ultraviolet spectrophotometer, with absorbance spectra ranging from 500 to 600 nm (Figure S39). Notably, there was a trend of gradual enhancement in fluorescence emission of the photodrugs as the alkyl chain length increased (Figure S38). The emission peaks ranged from 700 to 800 nm, reaching the near-infrared emission "biomedical" window with good tissue penetration, offering potential for future therapeutic applications. To further assess the ROS-generating capacity of the photodrugs, 2′,7′-dichlorodihydrofluorescein (DCFH) was used as an indicator of total ROS production. DCFH oxidizes to fluorescent 2',7'-Dichlorofluorescein (DCF), detectable by measuring green fluorescence at 525 nm. Fluorescence changes at 525 nm were recorded under white light irradiation (5 mW/cm^2) for 1 min for TC_n and TC_nT. It was observed that the total ROS production of TC_n decreased with increasing alkyl chain length, whereas the ROS production of TC_nT increased with increasing alkyl chain length (Figure 3D,G). This indicates that our molecular design effectively enhanced the ROS yield of the photodrugs, compared with the commercial photosensitizers Chlorin e6 (Ce6), rose bengal (RB), and methylene blue (MB).

Subsequently, to evaluate the types of ROS generated by the photodrugs under light irradiation, DHR123 was used as an indicator for detecting $O_2^{\bullet-}$, as $O_2^{\bullet-}$ radicals oxidize DHR123, transforming it from a nonfluorescent to a fluorescent state. As shown in Figure 3E,H, solutions of TC_n and TC_nT emitted bright fluorescence under white light irradiation (5 mW/cm^2), indicating their excellent capability for generating $O_2^{\bullet-}$. Additionally, ABDA was employed as a $^1O_2$ indicator. Upon irradiation, $^1O_2$ generated by the photodrugs oxidizes ABDA, disrupting its molecular structure and decreasing its absorbance. As shown in Figure 3F,I, TC_n and TC_nT exhibited significantly higher $^1O_2$ generation capacity, compared to the commercial photosensitizers (Ce6, RB, and MB). Taken together, the *in vitro* experimental results demonstrate that photodrugs TC_n and TC_nT can generate various types of ROS through both Type I and Type II photochemical processes, making them promising candidates for use in PDT therapy against pathogenic microorganisms.

3.3 | Fluorescence imaging of Gram-negative bacteria incubated with photodrugs

As described in the previous sections, based on the predictions by MD simulations, the staining of bacteria by these photodrugs was

15475905, 2026, 5, Downloaded from https://aiche.onlinelibrary.wiley.com/doi/10.1002/aic.70238 by Ewha Womans University Library, Wiley Online Library on [21/09/2026]. See the Terms and Conditions (https://onlinelibrary.wiley.com/terms-and-conditions) on Wiley Online Library for rules of use; OA articles are governed by the applicable Creative Commons License

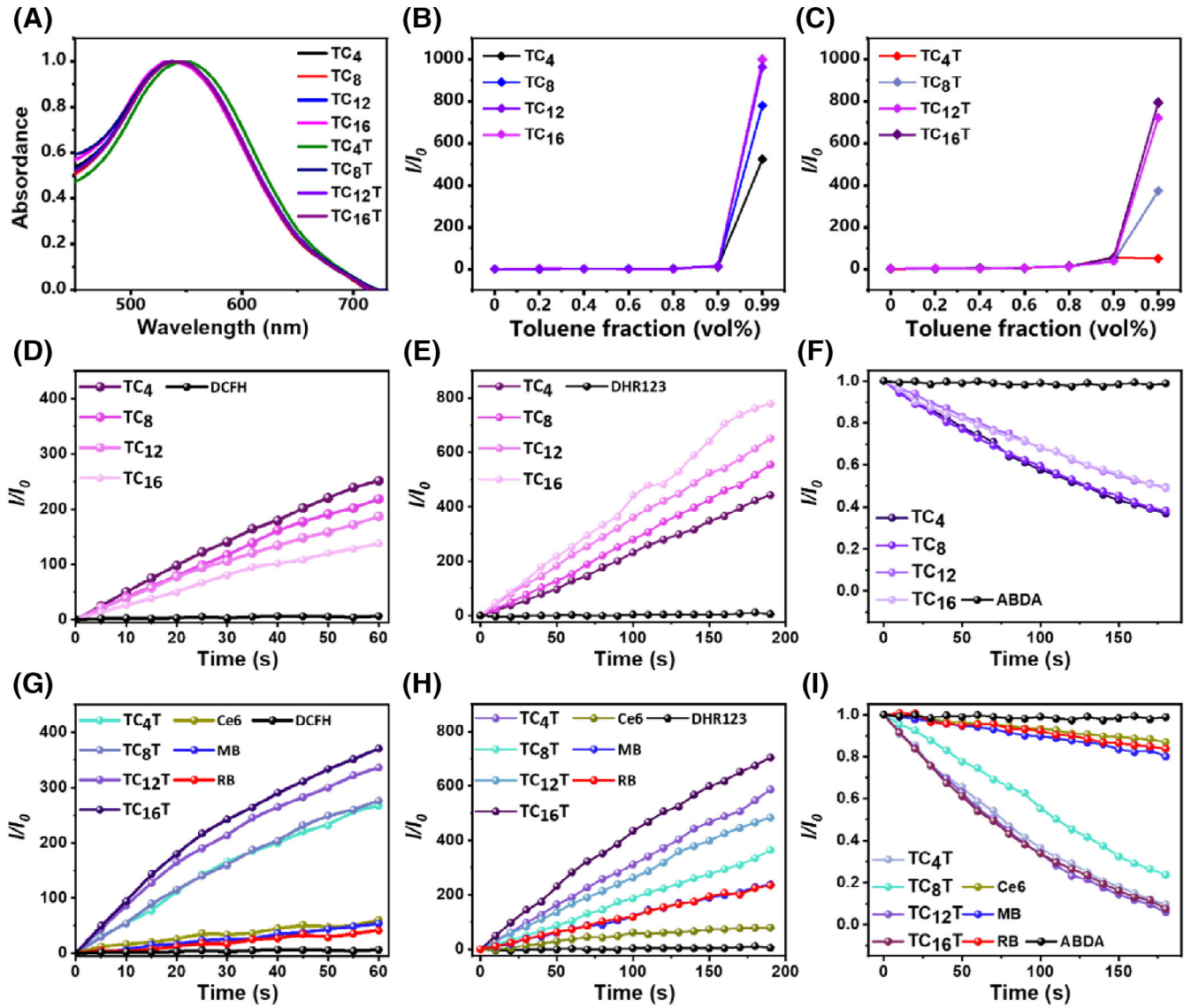


FIGURE 3 (A) Normalized absorption spectra of TC_4–TC_{16} and TC_4T–$TC_{16}T$ in DMSO. (B) and (C) Changes in maximum fluorescence intensity (I/I_0) of TC_4–TC_{16} and TC_4T–$TC_{16}T$ in DMSO with different toluene volume fractions (f_w). (D) and (G) Total reactive oxygen species (ROS) production of TC_4–TC_{16} and TC_4T–$TC_{16}T$ under white light irradiation. Relative changes in fluorescence intensity (I/I_0) of 2′,7′-dichlorodihydrofluorescein (DCFH) at 534 nm in 99% Phosphate Buffered Saline PBS/DMSO under 5 mW/cm^2 white light irradiation at different time points. (E) and (H) $O_2^{\bullet-}$ production of TC_4–TC_{16} and TC_4T–$TC_{16}T$ under white light irradiation. Relative changes in fluorescence intensity (I/I_0) of dihydrorhodamine 123 (DHR123) indicator at 534 nm in 90% PBS/DMSO under 5 mW/cm^2 white light irradiation at different time points. (F) and (I) $^1O_2$ production of TC_4–TC_{16} and TC_4T–$TC_{16}T$ under white light irradiation. Relative changes in 9,10-anthracenediyl-bis[methylene] dicarboxylic acid (ABDA) absorption (I/I_0) at 379 nm in 99% PBS/DMSO under 10 mW/cm^2 white light irradiation at different time points.

investigated further using CLSM. We selected *E. coli* as a classical model of Gram-negative bacteria to validate the transmembrane mechanism of photodrugs across Gram-negative bacterial membranes in comparison to the MD simulation results. As indicated in Figure 4, fluorescence images of TC_n-incubated *E. coli* showed a gradual decrease in fluorescence intensity with increasing molecular size. This observation is consistent with the MD simulation findings, indicating that the transmembrane ability of photodrug TC_n to cross Gram-negative bacteria diminishes as the molecular size increases. More notably, when *E. coli* was co-incubated with TC_nT, TC_8T exhibited brighter fluorescence at the same time point. This is also consistent with the MD simulation conclusion that the molecular size of TC_8T is better matched to the membrane structure of Gram-negative bacteria, facilitating its embedding within the bacterial membrane, so that TC_8T is more membrane-disruptive, and then the more TC_8T molecules permeate into the cells.

These results, in conjunction with MD simulations, indicate that the ability of photodrugs TC_n to cross membranes depends on molecular size. The difference is that TC_nT enhances the embedding of the molecules in the bacteria membrane by adjusting the alkyl chain

15475905, 2026, 5, Downloaded from https://aiche.onlinelibrary.wiley.com/doi/10.1002/aic.70238 by Ewha Womans University Library, Wiley Online Library on [21/09/2026]. See the Terms and Conditions (https://onlinelibrary.wiley.com/terms-and-conditions) on Wiley Online Library for rules of use; OA articles are governed by the applicable Creative Commons License

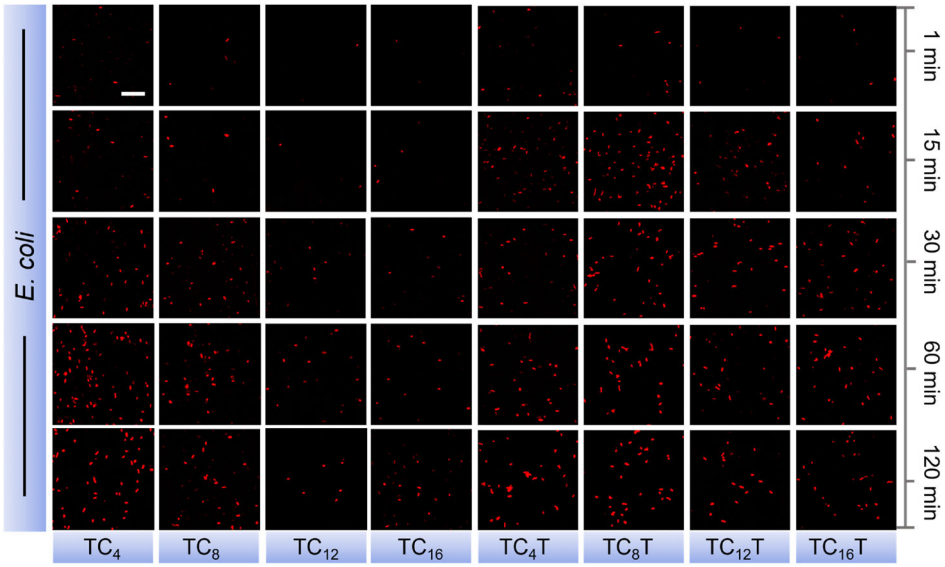


FIGURE 4 Fluorescence intensity changes of various photodrugs (2 μM) incubated with *Escherichia coli* at different time points (1, 15, 30, 60, and 120 min). Scale bar: 20 μm.

length to match the thickness of the bacterial membrane enhances the embedding of the molecule in the cell membrane, while dual-cation charges improve its ability to bind to the membrane structure and enhance membrane perturbation capabilities. Among the photodrugs, TC_8T better matched and embedded into the membranes of *E. coli* thus promoting the accumulation of more TC_8T penetrating the cell membrane inside the bacteria and reached saturation at about 60 min (Figure S40). Additionally, under photoirradiation, TC_8T produced a significant amount of ROS inside the bacteria (Figure S41), further contributing to the effective killing of drug-resistant bacteria.

3.4 | *In vitro* bacterial/fungal inhibition mechanism of photodrugs

As mentioned above, the ability of the photodrugs to cross the microbial membrane using fluorescence imaging was systematically studied. Building on this foundation, light intervention activates the photosensitizing toxicity of the photodrugs, producing highly toxic ROS that oxidize the phospholipid membrane or other cellular structures, thereby enhancing antimicrobial efficiency. In the subsequent experiment, the antibacterial performances of TC_n and TC_nT under white light irradiation were evaluated. Consistent with our CLSM findings, we first investigated the antimicrobial mechanisms of TC_n and TC_nT using *E. coli* as a Gram-negative bacterial model. Scanning electron microscopy was employed to observe the damage of *E. coli* following photodrug treatment. Specifically, *E. coli* was cultured with photodrugs TC_n and TC_nT (2 μM) for 1 h and then irradiated with white light (10 mW/cm^2) for 10 min. As shown in Figure 5A, untreated *E. coli* exhibited complete and uniform rod-shaped cells with smooth and intact bacterial membranes. In contrast, after co-incubation with photodrugs *plus* light irradiation, the bacterial membranes appeared fragmented, resulting in leakage of cellular contents and bacterial fragmentation. Notably, *E. coli* treated with photodrug TC_8T showed more pronounced disruption of the bacterial membrane. And, as shown in Figure S42, bacterial membranes were most significantly affected by TC_8T when *E. coli* were co-incubated with the photodrugs without light irradiation, leading to leakage of cell contents and accelerated uptake of the photodrugs.

To further investigate the differences in the macroscopic inhibitory properties of photodrugs with varying alkyl chain lengths and cationic charges, *E. coli* was treated with different concentrations of TC_n and TC_nT for 1 h, followed by white light irradiation (10 and 25 mW/cm^2) for 10 min. The actual inhibition efficiency was determined using the plate spreading method. As depicted in Figures 5B–D and S43, the inhibitory effects of TC_4 to TC_{16} weakened with increasing alkyl chain length, which was consistent with the CLSM and MD simulation results. In contrast, among the dimeric photodrugs TC_nT, TC_8T demonstrated superior antibacterial activity. This enhanced performance is attributed to its suitable molecular size, which better matches the bacterial membrane structure, and the membrane disruption driven by dual-cationic charges, facilitating more rapid embedding into the bacterial membrane at very low concentrations.

Facing the growing crisis of drug resistance in Gram-negative bacteria, the dimeric cationic photodrug TC_8T, identified through MD simulations, was further evaluated for its inhibitory activity against multidrug-resistant strains. We treated drug-resistant *A. baumannii*, *K. pneumoniae*, and *ESBL E. coli* with TC_8T. As illustrated in Figure 6A,B, TC_8T effectively inhibited the proliferation of multiple drug-resistant bacteria, as evidenced by plate coating experiments. This exciting result demonstrates that MD simulations can successfully optimize ideal photodrugs against multi-resistant bacteria, thereby counteracting the growing issue of bacterial resistance and providing non-antibiotic therapeutic options for the clinical management of antibiotic resistance.

Additionally, further analysis using the plate coating method, under the same treatment conditions, commercial dyes (Ce6, MB, and RB) did not have a significant inhibitory effect (Figure S44). Based on these experimental results, we conclude that the dimeric photodrug TC_8T possesses desirable antimicrobial properties. The integration of MD simulations in the design process was instrumental in achieving

15475905, 2026, 5, Downloaded from https://aiche.onlinelibrary.wiley.com/doi/10.1002/aic.70238 by Ewha Womans University Library, Wiley Online Library on [21/09/2026]. See the Terms and Conditions (https://onlinelibrary.wiley.com/terms-and-conditions) on Wiley Online Library for rules of use; OA articles are governed by the applicable Creative Commons License

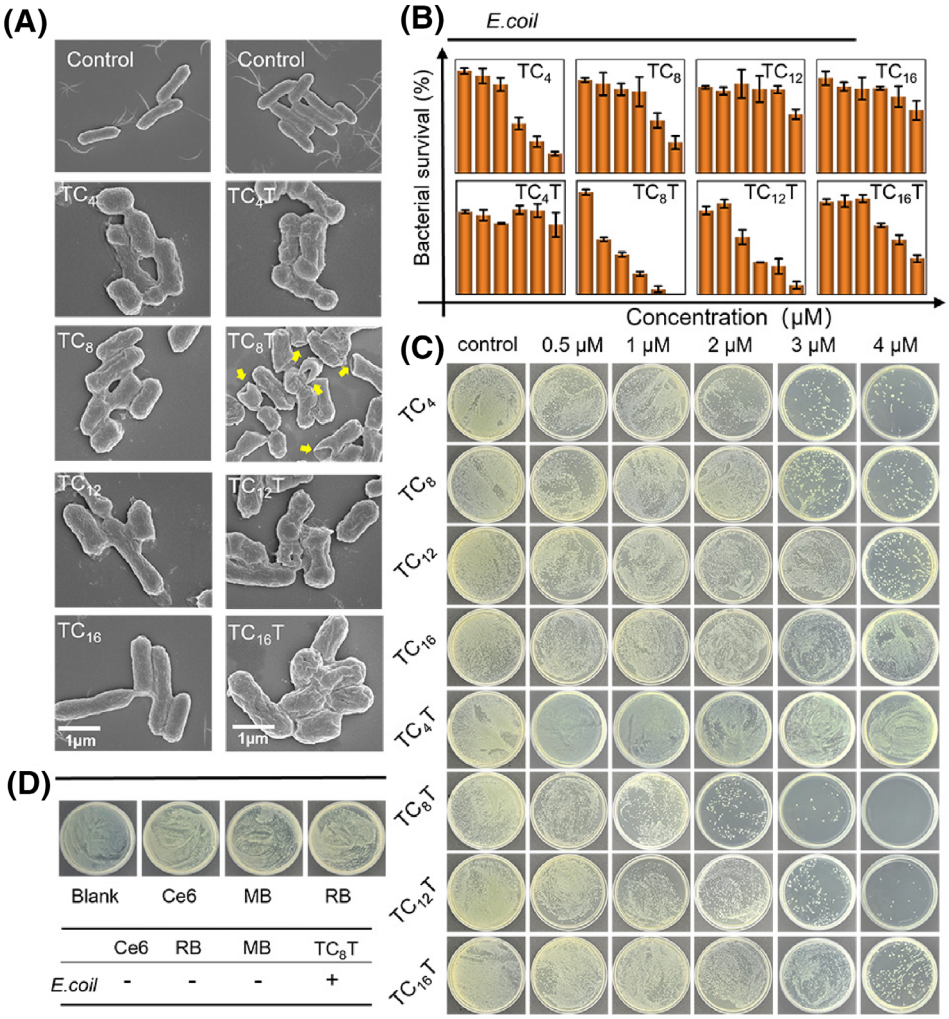


FIGURE 5 (A) Scanning electron microscope images of *Escherichia coli* morphology after incubation with TC_{4-16} or TC_4T–$TC_{16}T$ (2 μM) and subsequent light exposure. (B) Statistical analysis of *E. coli* photodynamic killing data presented in panel (C). (C) Inactivation of *E. coli* by white light irradiation (10 mW/cm^2) for 10 min following incubation with indicated concentrations of TC_{4-16} or TC_4T–$TC_{16}T$ for 1 h. (D) Photodynamic inactivation of *E. coli* by incubation with commercial photosensitizers (Ce6, MB, and RB; 2 μM) for 1 h and subsequent white light irradiation (10 mW/cm^2) for 10 min ("−" represents poor antibacterial effect; "+" represents excellent antibacterial effect).

this outcome, validating TC_8T as a potent antimicrobial agent with combatting drug-resistant bacteria.

3.5 | *In vivo* PDT

Building on the excellent *in vitro* photodynamic antibacterial outcomes of the dimeric photodrug TC_8T, we further evaluated its *in vivo* performance (Figure 7A). The construction of wound infection models on the backs of mice inoculated with *E. coli* was then undertaken. Photographs of the wound infections were taken on Days 1, 4, 7, and 10 (Figure 7B), and the wound healing process was monitored to assess the *in vivo* antimicrobial properties of TC_8T. All wounds inoculated with the strains became infected and suppurated on the first day. Compared with control groups, the experimental groups treated with photodrug TC_8T *plus* white light irradiation exhibited a significant decrease in the wound infection area by Day 10, indicating that TC_8T effectively inhibited microbial infections in the wounds. Additionally, on the 10th day post-inoculation, tissue fluid from the infected areas was collected for plate colony counting to further evaluate the inhibitory effect of TC_8T (Figure 7C). As observed in Figure 7C, the number of colonies in the control group exceeded 2×10^8 CFU, whereas no significant colonies were detected in the TC_8T-treated experimental group. This result clearly confirms that TC_8T possesses significant microbial inhibitory effects in wound infection models.

During the treatment process, the weight changes of mice in both the experimental and control groups were also recorded (Figure S45). No significant differences were observed, suggesting that TC_8T has good biocompatibility and does not adversely affect the health of the mice. On the 10th day, the mice were euthanized to obtain infected tissues for hematoxylin and eosin staining to further evaluate the effect of TC_8T on the infected tissues. As seen in Figure 7D, the infected skin tissues in the control group were infiltrated by a large number of neutrophils, along with an increase in fibroblasts and capillary reconstruction following TC_8T administration and photoirradiation. These observations suggested that TC_8T effectively inhibited the pathogenicity of wound bacteria, promoting tissue regeneration and recovery. Additionally, the biosafety of TC_8T-treated experimental was confirmed via Hematoxylin and eosin stains (H&E) staining of the major tissues and hemolysis assay, which showed that no significant morphological changes of these organs and no obvious changes for the blood parameters were observed after treatments (Figures S46 and S47).

To explore the potential clinical application of TC_8T, we established an animal model of mixed bacterial (*S. aureus*, 2×10^8 CFU;

15475905, 2026, 5, Downloaded from https://aiche.onlinelibrary.wiley.com/doi/10.1002/aic.70238 by Ewha Womans University Library, Wiley Online Library on [21/09/2026]. See the Terms and Conditions (https://onlinelibrary.wiley.com/terms-and-conditions) on Wiley Online Library for rules of use; OA articles are governed by the applicable Creative Commons License

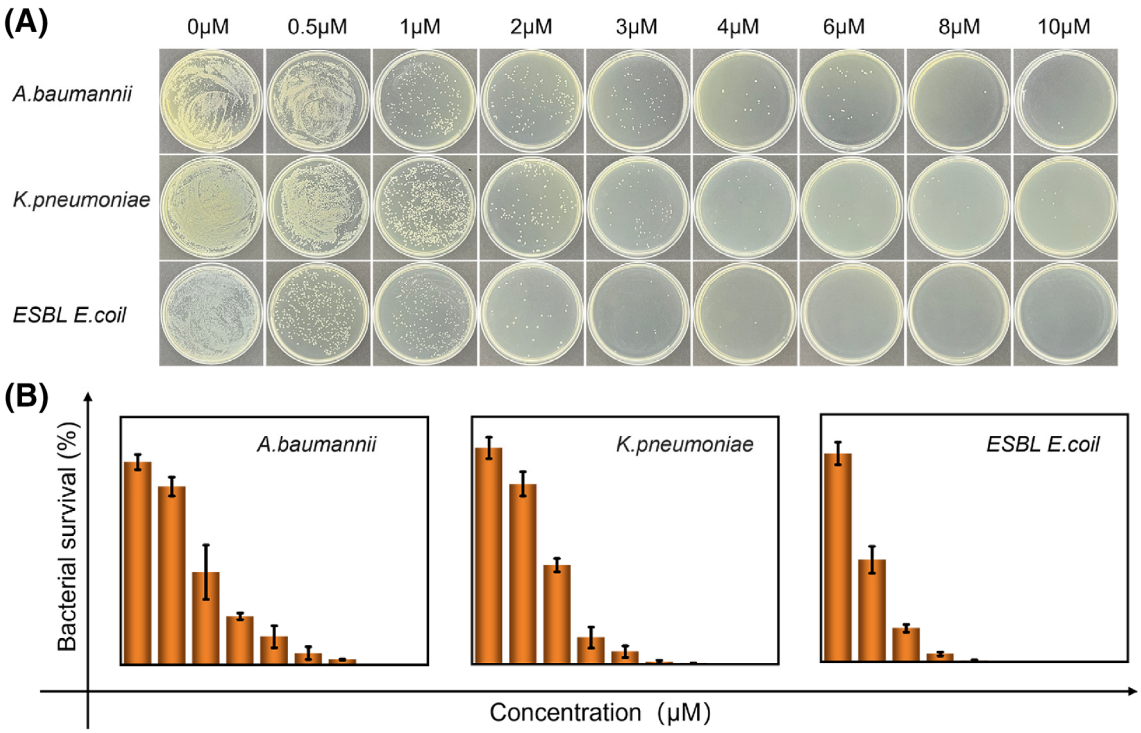
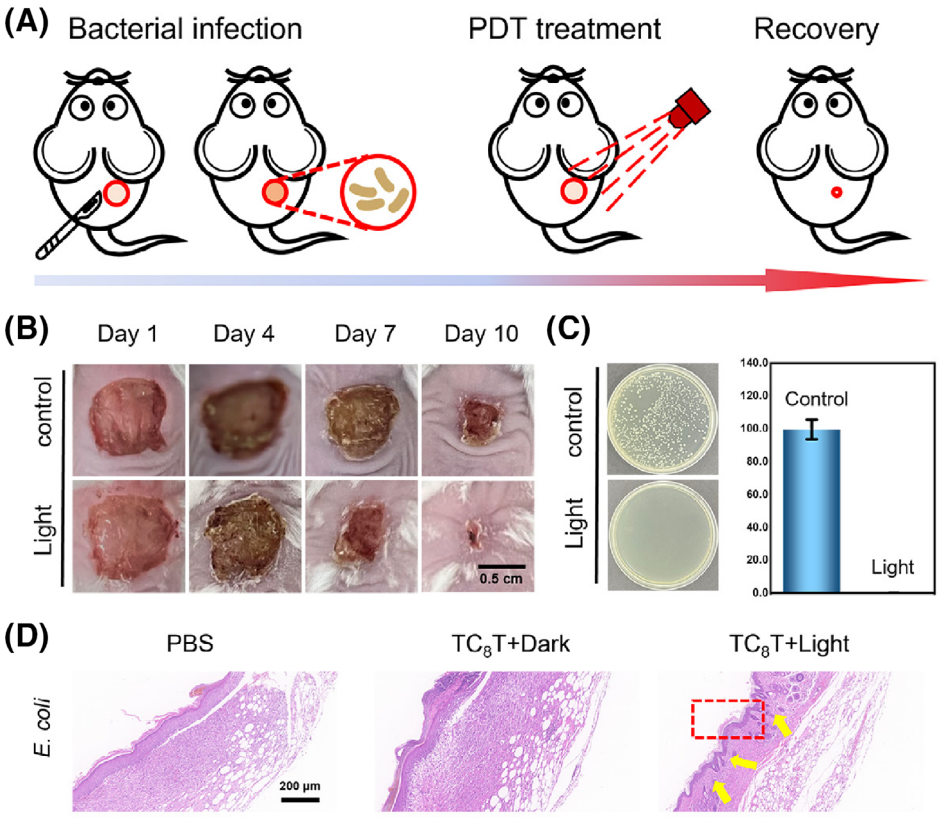


FIGURE 6 (A) Photodynamic inhibition of *Acinetobacter baumannii*, *Klebsiella pneumoniae*, and *ESBL Escherichia coli* by incubation with TC_8T for 1 h followed by white light irradiation (50 mW/cm^2) for 10 min. (B) Statistical analysis of photodynamic killing data for *A. baumannii*, *K. pneumoniae*, and extended-spectrum beta-lactamase (*ESBL*) *E. coli* presented in panel (A).

FIGURE 7 (A) The murine models of wound infection. (B) Photographs of mice wounds after treatment with photodrug TC_8T (2 μM) *plus* white light irradiation at different time points (1, 4, 7, and 10 days). (C) Microbial plate cultures of wound samples (the coated agar plates, left) and the corresponding statistical analysis of antibacterial activity (right) on Day 10 following treatments with photodrugs. Error bars represent standard deviation, $n = 3$.
(D) Hematoxylin and eosin staining of wound tissue after 10 days of various treatments. PDT, photodynamic therapy.



15475905, 2026, 5, Downloaded from https://aiche.onlinelibrary.wiley.com/doi/10.1002/aic.70238 by Ewha Womans University Library, Wiley Online Library on [21/09/2026]. See the Terms and Conditions (https://onlinelibrary.wiley.com/terms-and-conditions) on Wiley Online Library for rules of use; OA articles are governed by the applicable Creative Commons License

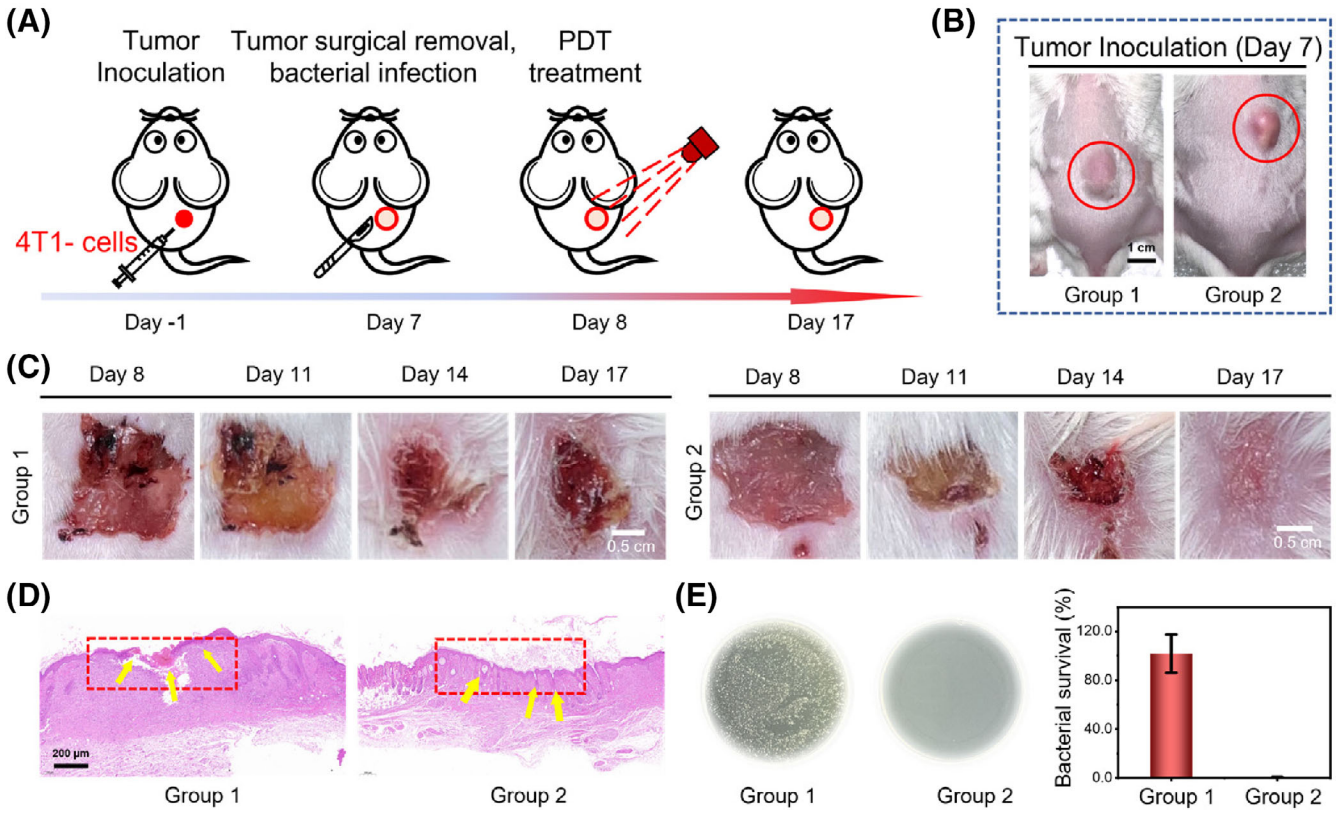


FIGURE 8 (A) Schematic illustration of mixed bacterial and fungal infections in mice following surgical resection of tumors and the photodynamic therapy (PDT) process. (B) Photographs of mouse tumors. (C) Wound changes in mice in Group 1 and Group 2. (D) Hematoxylin and eosin staining analysis of wound skin on Day 17 of treatment. (E) Microbial plate cultures of wound samples (the coated agar plates, left) and the corresponding statistical analysis of antibacterial activity (right) on Day 9 following treatments with Group 1 and Group 2. Error bars represent standard deviation, $n = 3$ (Group 1: Mixed wound infection with *Escherichia coli*, *Staphylococcus aureus*, and *Candida albicans* without light irradiation; Group 2: Mixed wound infection with *E. coli*, *S. aureus*, and *C. albicans* with white light irradiation (10 mW/cm^2, 10 min).

E. coli, 2×10^8 CFU) and fungal (*C. albicans*, 2×10^8 CFU) infections in mice following surgical resection of tumors (Figure 8A,B) to evaluate its antimicrobial efficiency. Specifically, after establishing 4T1-bearing tumor-bearing mice, the solid tumors were resected, and the wounds were inoculated with a mixture solution of *S. aureus*, *E. coli*, and *C. albicans* to simulate the real condition of multiple microbial infections post-surgery. On Day 8 (1 day after tumor resection), a purulent infection appeared on the wound surfaces (Figure 8C), indicating successful colonization by the pathogenic microorganisms.

Subsequently, the wounds were treated with TC_8T (2 μM) solution *plus* white light irradiation (10 mW/cm^2) for 10 min, and photographs of the wounds were taken at various time points to document the treatment effects. By Day 17, the wounds in the untreated group (Group 1) remained severely infected, whereas the wounds of the TC_8T-treated mice (Group 2) were nearly healed. These results indicate that the administration of TC_8T under photoirradiation effectively eradicated the cross-infection of multiple bacteria and fungi in surgical wounds, thereby promoting wound healing.

Moreover, tissue fluid from the infected sites was collected on Day 17 for plate colony counting (Figure 8E). The control group (Group 1) exhibited a high colony count of 2×10^8 CFU, whereas no obvious colonies were observed in the TC_8T-treated group (Group 2), clearly demonstrating that TC_8T significantly inhibited microbial infections in surgical wounds in the presence of white light irradiation. Additionally, tissues from the surgical sites of mice on Day 17 were stained with hematoxylin and eosin to assess histological changes (Figures 8D and S48). As shown in Figure 8D, Group 1 exhibited significant inflammatory cell infiltration, whereas Group 2 displayed reduced inflammatory cell infiltration and accelerated tissue reconstruction. These findings firmly demonstrate the efficacy of the dimeric photodrug TC_8T in inhibiting cross-infection after tumor surgery.

Based on these results, the dimeric cationic photodrug TC_8T, identified through MD simulations, demonstrated excellent *in vivo* antibacterial treatment effects via phototherapy. This provides an additional non-antibiotic drug option for clinical applications, addressing the pressing issue of antibiotic resistance.

4 | CONCLUSIONS

In conclusion, we developed monomeric photodrugs (TC_n) and dimeric photodrugs (TC_nT). The intrinsic transmembrane mechanisms of TC_n and TC_nT were systematically verified through a range of methods, including MD simulations, fluorescence confocal imaging, *in vitro*

15475905, 2026, 5, Downloaded from https://aiche.onlinelibrary.wiley.com/doi/10.1002/aic.70238 by Ewha Womans University Library, Wiley Online Library on [21/09/2026]. See the Terms and Conditions (https://onlinelibrary.wiley.com/terms-and-conditions) on Wiley Online Library for rules of use; OA articles are governed by the applicable Creative Commons License

bacterial inhibition assays, and bacterial morphology observations. Through this comprehensive evaluation, we identified the dimeric cationic photodrug TC_8T as the most effective antibacterial agent. The molecular size of TC_8T optimally matches the bacterial membrane structure, facilitating its embedding into the membrane. Its dimeric cationic structure effectively disrupts the arrangement of the phospholipid bilayer, allowing free TC_8T outside the membrane to accumulate inside the bacteria more rapidly over the bacterial membrane barrier. In contrast, the smaller photodrug TC_4T struggles to penetrate the bacterial membrane, while $TC_{12}T$ and $TC_{16}T$, although capable of embedding into the membrane, exhibit reduced membrane perturbation with increasing alkyl chain lengths. Furthermore, the ROS generated upon light irradiation after TC_nT embedding further damage the bacterial membrane, amplifying the differences in embedding abilities among the various photodrugs. Importantly, *in vitro* bacterial inhibition experiments demonstrated that TC_8T possesses excellent inhibitory effects against *E. coli*, *A. baumannii*, *K. pneumoniae*, and *ESBL E. coli* as well as outstanding inhibitory activity against a wide range of drug-resistant bacteria. The molecular size-matching effect of TC_8T synergizes with its cationic photodynamic-mediated inhibition mechanism, enhancing its antibacterial efficacy. This dual-cationic charges and a matched molecular size bacterial inhibition mechanism were further validated in three different bacterial wound infection models in mice.

Moreover, the dimeric photodrug TC_8T exhibited exceptional performance in photodynamic antibacterial treatment of mixed bacterial infections in mice following tumor resection, promoting the reconstruction of wound skin tissue. This study highlights the significant potential of using MD simulations to optimize novel bacteriostatic photodrugs and provides a novel approach for designing effective dimeric cationic photodrugs. By integrating molecular size optimization and dual-cationic structures, TC_8T offers a promising non-antibiotic therapeutic option to address the pressing issue of antibiotic resistance in clinical settings.

AUTHOR CONTRIBUTIONS

Lei Hao: Conceptualization, methodology, investigation, visualization, writing—original draft; **Yeonho Song**: Methodology, visualization, writing—review and editing; **Cheng Zhang**: Methodology; **Yumei Wang**: Investigation; **Haoying Ge**: Methodology; **Wen Sun**: Writing—review and editing; **Jingyun Wang**: Conceptualization, writing—review and editing, funding acquisition; **Jun Soo Kim**: Methodology, visualization, writing—review and editing, funding acquisition; **Xiaojun Peng**: Writing—review and editing, funding acquisition; **Juyoung Yoon**: Conceptualization, writing—review and editing, funding acquisition; **Haidong Li**: Conceptualization, investigation, visualization, writing—review and editing, funding acquisition.

ACKNOWLEDGMENTS

This work was supported by the National Natural Science Foundation of China (22378050, 22378051, and 22090011), the National Key Research and Development Program of China (2023YFB3810300), the Liaoning Provincial Science and Technology Joint Fund (2023JH2/101700296), the Fundamental Research Funds for the Central Universities (DUT24ZD117 and DUT24LAB105), and the National Research Foundation of Korea (MSIT) (RS-2023-00217701, 2022R1A2C3005420, and 2020R1A5A2019210).

CONFLICT OF INTEREST STATEMENT

The authors declare no conflict of interest.

DATA AVAILABILITY STATEMENT

Numerical data for the absorbance spectra from Figure 3A; line plot of Figure 3B,C based on Figure S38, and absorbance and fluorescence spectra from Figure 3D–I, are provided in Supporting Information S1.

ORCID

Wen Sun https://orcid.org/0000-0003-4316-5350
Xiaojun Peng https://orcid.org/0000-0002-8806-322X
Juyoung Yoon https://orcid.org/0000-0002-1728-3970
Haidong Li https://orcid.org/0000-0002-2721-0337

REFERENCES

1. Kim H, Lee YR, Jeong H, et al. Photodynamic and photothermal therapies for bacterial infection treatment. *Smart Mol*. 2023;1(1):e20220010.
2. GBD 2021 Antimicrobial Resistance Collaborators. Global burden of bacterial antimicrobial resistance 1990–2021: a systematic analysis with forecasts to 2050. *Lancet*. 2024;404(10459):1199-1226.
3. Wang Z, Wu A, Cheng W, et al. Adoptive macrophage directed photodynamic therapy of multidrug-resistant bacterial infection. *Nat Commun*. 2023;14(1):7251.
4. Okeke IN, de Kraker MEA, Van Boeckel TP, et al. The scope of the antimicrobial resistance challenge. *Lancet*. 2024;403(10442):2426-2438.
5. Hu H, Wang H, Yang Y, Xu JF, Zhang X. A bacteria-responsive porphyrin for adaptable photodynamic/photothermal therapy. *Angew Chem Int Ed*. 2022;61(23):e202200799.
6. Huo J, Jia Q, Huang H, et al. Emerging photothermal-derived multimodal synergistic therapy in combating bacterial infections. *Chem Soc Rev*. 2021;50(15):8762-8789.
7. Kang M, Zhou C, Wu S, et al. Evaluation of structure–function relationships of aggregation-induced emission luminogens for simultaneous dual applications of specific discrimination and efficient photodynamic killing of Gram-positive bacteria. *J Am Chem Soc*. 2019;141(42):16781-16789.
8. Dunne M, Hupfeld M, Klumpp J, Loessner MJ. Molecular basis of bacterial host interactions by Gram-positive targeting bacteriophages. *Viruses*. 2018;10(8):397.
9. Li H, Kim H, Han J, Nguyen VN, Peng X, Yoon J. Activity-based smart AIEgens for detection, bioimaging, and therapeutics: recent progress and outlook. *Aggregate*. 2021;2(4):e51.
10. Li H, Kim H, Xu F, et al. Correction: activity-based NIR fluorescent probes based on the versatile hemicyanine scaffold: design strategy, biomedical applications, and outlook. *Chem Soc Rev*. 2022;51(5):1836.
11. Sun Z, Ma L, Sun X, Sloan AJ, O'Brien-Simpson NM, Li W. The overview of antimicrobial peptide-coated implants against oral bacterial infections. *Aggregate*. 2023;4(3):e309.
12. Wu M, Liu X, Chen H, et al. Activation of pyroptosis by membrane-anchoring AIE photosensitizer design: new prospect for photodynamic cancer cell ablation. *Angew Chem Int Ed*. 2021;60(16):9093-9098.
13. Wu X, Yang M, Kim JS, et al. Reactivity differences enable ROS for selective ablation of bacteria. *Angew Chem Int Ed Engl*. 2022;61(17):e202200808.
14. Wu Y, Li J, Shen Z, et al. Double-pronged antimicrobial agents based on a donor-π-acceptor type aggregation-induced emission luminogen. *Angew Chem Int Ed*. 2022;61(47):e202212386.

15475905, 2026, 5, Downloaded from https://aiche.onlinelibrary.wiley.com/doi/10.1002/aic.70238 by Ewha Womans University Library, Wiley Online Library on [21/09/2026]. See the Terms and Conditions (https://onlinelibrary.wiley.com/terms-and-conditions) on Wiley Online Library for rules of use; OA articles are governed by the applicable Creative Commons License

15. Qi G, Tang Y, Shi L, Zhuang J, Liu X, Liu B. Capsule shedding and membrane binding enhanced photodynamic killing of Gram-negative bacteria by a unimolecular conjugated polyelectrolyte. *Nano Lett*. 2023;23(22):10374-10382.
16. Wu MY, Xu X, Hu R, et al. A membrane-targeted photosensitizer prevents drug resistance and induces immune response in treating candidiasis. *Adv Sci*. 2023;10(35):2207736.
17. Sun B, Wang X, Ye Z, et al. Designing single-atom active sites on sp2-carbon linked covalent organic frameworks to induce bacterial ferroptosis-like for robust anti-infection therapy. *Adv Sci*. 2023;10(13):2207507.
18. Liu F, Liu J, Gong J, et al. Complex-mediated nucleophilic aromatic substitution with aryl nitriles to realize intramolecular flapping-restricted D-A AIEgens for bioimaging. *Smart Mol*. 2024;3:e20240039.
19. Zeng S, Wang Z, Chen C, et al. Construction of Rhodamine-based AIE photosensitizer hydrogel with clinical potential for selective ablation of drug-resistant Gram-positive bacteria in vivo. *Adv Healthc Mater*. 2022;11(17):2200837.
20. Zhang L, Hu C, Sun M, et al. BODIPY-functionalized natural polymer coatings for multimodal therapy of drug-resistant bacterial infection. *Adv Sci*. 2023;10(14):e2300328.
21. Zheng L, Zhu Y, Sun Y, et al. Flexible modulation of cellular activities with cationic photosensitizers: insights of alkyl chain length on reactive oxygen species antimicrobial mechanisms. *Adv Mater*. 2023;35(35):2302943.
22. Zheng L, Li J, Yu M, et al. Molecular sizes and antibacterial performance relationships of flexible ionic liquid derivatives. *J Am Chem Soc*. 2020;142(47):20257-20269.
23. Sharma P, Parthasarathi S, Patil N, et al. Assessing barriers for antimicrobial penetration in complex asymmetric bacterial membranes: a case study with thymol. *Langmuir*. 2020;36(30):8800-8814.
24. Wadhwa R, Yadav NS, Katiyar SP, et al. Molecular dynamics simulations and experimental studies reveal differential permeability of withaferin-A and withanone across the model cell membrane. *Sci Rep*. 2021;11(1):2352.
25. Gnanasekar S, Kasi G, He X, Zhang K, Xu L, Kang ET. Recent advances in engineered polymeric materials for efficient photodynamic inactivation of bacterial pathogens. *Bioact Mater*. 2023;21:157-174.
26. Ye Z, Fu L, Li S, et al. Synergistic collaboration between AMPs and non-direct antimicrobial cationic peptides. *Nat Commun*. 2024;15(1):7319.
27. Ren E, Zhang C, Li D, Pang X, Liu G. Leveraging metal oxide nanoparticles for bacteria tracing and eradicating. *View*. 2020;1(3):20200052.
28. Wang R, He M, Zhang Z, et al. Photodynamic therapy promotes hypoxia-activated nitrogen mustard drug release. *Smart Mol*. 2024;2(3):e20240010.
29. Nguyen V-N, Zhao Z, Tang BZ, Yoon J. Organic photosensitizers for antimicrobial phototherapy. *Chem Soc Rev*. 2022;51(9):3324-3340.
30. Hou Y, Li J, Jiang G, et al. Synergistic inter- and intramolecular aggregation of dimeric cyanine dyes affords highly efficient in vivo self-delivery and photothermal therapy. *Adv Funct Mater*. 2024;34(32):2316452.
31. Li H, Yang M, Kim JS, et al. Structure-oriented design strategy to construct NIR AIEgens to selectively combat Gram (+) multidrug-resistant bacteria in vivo. *Biomaterials*. 2022;286:121580.
32. Li H, Zhang L, Han J, et al. Molecular structural evolution of near-infrared cationic aggregation-induced emission luminogens: preclinical antimicrobial pathogens activities and tissues regeneration. *CCS Chem*. 2022;4(2):487-500.
33. McCain J, Martínez SR, Fungo F, Sakaya A, Cosa G. Two-pronged dormant photosensitizer-antibiotic bacterial inactivation: mechanism, dosage, and cellular evolution visualized at the single-cell level. *J Am Chem Soc*. 2023;145:28124-28136.
34. Wang P, Wu B, Li M, et al. Lysosome-targeting aggregation-induced emission nanoparticle enables adoptive macrophage transfer-based precise therapy of bacterial infections. *ACS Nano*. 2023;17(11):10365-10375.
35. Xia F, Guo B, Zhao Y, et al. Type I photosensitizer targeting glycans: overcoming biofilm resistance by inhibiting the two-component system, quorum sensing, and multidrug efflux. *Adv Mater*. 2023;35(52):2309797.
36. Wang W, Wu F, Zhang Q, et al. Aggregation-induced emission nanoparticles for single near-infrared light-triggered photodynamic and photothermal antibacterial therapy. *ACS Nano*. 2022;16(5):7961-7970.
37. Hu H, Zhang YY, Ma H, et al. A supramolecular naphthalene diimide radical anion with efficient NIR-II photothermal conversion for *E. coli*-responsive photothermal therapy. *Angew Chem Int Ed*. 2023;62(41):e202308513.
38. Jiang J, Lv X, Cheng H, et al. Type I photodynamic antimicrobial therapy: principles, progress, and future perspectives. *Acta Biomater*. 2024;177:1-19.
39. Mu S, Zhu Y, Wang Y, et al. Cationic polysaccharide conjugates as antibiotic adjuvants resensitize multidrug-resistant bacteria and prevent resistance. *Adv Mater*. 2022;34(41):2204065.
40. Lindahl E, Abraham MJ, Hess B, van der Spoel D. GROMACS 2020.4 manual (2020). doi:10.5281/zenodo.4054996
41. Abraham MJ, Murtola T, Schulz R, et al. GROMACS: high performance molecular simulations through multi-level parallelism from laptops to supercomputers. *SoftwareX*. 2015;1-2:19-25.
42. Humphrey W, Dalke A, Schulten K. VMD: visual molecular dynamics. *J Mol Graph*. 1996;14(1):33-38.
43. Hong C, Tieleman DP, Wang Y. Microsecond molecular dynamics simulations of lipid mixing. *Langmuir*. 2014;30(40):11993-12001.
44. Hwang H, Paracini N, Parks JM, Lakey JH, Gumbart JC. Distribution of mechanical stress in the *Escherichia coli* cell envelope. *Biochim Biophy Acta*. 2018;1860(12):2566-2575.
45. Lee J, Cheng X, Swails JM. CHARMM-GUI input generator for NAMD, GROMACS, AMBER, OpenMM, and CHARMM/OpenMM simulations using the CHARMM36 additive force field. *J Chem Theory Comput*. 2016;12:405-413.
46. Jo S, Kim T, Iyer VG, Im W. CHARMM-GUI: a web-based graphical user interface for CHARMM. *J Comput Chem*. 2008;29(11):1859-1865.
47. Klauda JB, Venable RM, Freites JA, et al. Update of the CHARMM all-atom additive force field for lipids: validation on six lipid types. *J Phys Chem B*. 2010;114(23):7830-7843.
48. Vanommeslaeghe K, MacKerell AD. Automation of the CHARMM general force field (CGenFF) I: bond perception and atom typing. *J Chem Inf Model*. 2012;52(12):3144-3154.
49. Grossfield A. WHAM: the weighted histogram analysis method, version 2.0.11. Accessed March 15, 2024. http://membrane.urmc.rochester.edu/content/wham
50. Lee J, Cheng X, Swails JM, et al. CHARMM-GUI input generator for NAMD, GROMACS, AMBER, OpenMM, and CHARMM/OpenMM simulations using the CHARMM36 additive force field. *Chem Theory Comput*. 2016;12:405-413.

SUPPORTING INFORMATION

Additional supporting information can be found online in the Supporting Information section at the end of this article.

How to cite this article: Hao L, Song Y, Zhang C, et al. A rational strategy to optimize photodrugs by Molecular Dynamics simulations for killing drug-resistant Gram-negative bacteria. *AIChE J*. 2026;72(5):e70238. doi:10.1002/aic.70238

15475905, 2026, 5, Downloaded from https://aiche.onlinelibrary.wiley.com/doi/10.1002/aic.70238 by Ewha Womans University Library, Wiley Online Library on [21/09/2026]. See the Terms and Conditions (https://onlinelibrary.wiley.com/terms-and-conditions) on Wiley Online Library for rules of use; OA articles are governed by the applicable Creative Commons License